Aeronautical Journal, 2009, Volume 113, Issue 1149, pp727-738

Simulation of Wake Vortex Effects for UAVs in Close Formation Flight

Deborah Saban, James F. Whidborne, Alastair Cooke
Department of Aerospace Sciences
Cranfield University
Cranfield, UK

Abstract

This paper addresses the development of multiple UAV deployment simulation models that include representative aerodynamic cross-coupling effects. Applications may include simulations of autonomous aerial refuelling and formation flying scenarios. A novel wake vortex model has been developed and successfully integrated within a Matlab/Simulink simulation environment. The wake vortex model is both sufficiently representative to support studies of aerodynamic interaction between multiple air vehicles, and straightforward enough to be used within real time or near real time air-to-air simulations. The model integration process is described, and computational results of a two-vehicle-formation flight are presented.

Nomenclature

b	wing span
h	distance from point P to the vortex branch line
$\mathbf{n}$	unit vector in the normal direction
n_{seg}	number of discretisation segments
p	body roll rate
q	body pitch rate
r	body yaw rate
r_c	vortex core radius
V	air-vehicle airspeed
$\mathbf{V}$	air-vehicle velocity vector
$\mathbf{Vi}$	induced translational wind velocity vector
$\widetilde{\mathbf{Vi}}$	effective induced translational wind velocity vector
x_{rel}	x-component of the relative distance between two UAVs in formation
y_{rel}	y-component of the relative distance between two UAVs in formation
z_{rel}	z-component of the relative distance between two UAVs in formation

Greek symbols

α	angle of attack
β	angle of sideslip
Γ	vortex strength
δ	dihedral angle
ε	taper ratio
θ	pitch attitude; angular variable
λ	aspect ratio
ν	kinematic viscosity of the air
τ	age of the vortex branch
ϕ	bank angle
φ	sweepback angle at 1/4-chord
ψ	heading angle
$\widetilde{\boldsymbol{\omega}_i}$	effective induced rotational wind velocity vector

Subscripts

j, k	variable number
x, y, z	components of a vector in the x, y, z axes
Δ	incremental quantity

Introduction

The development of new and existing technologies, facilities, procedures and protocols is needed to permit the safe and routine operation of uninhabited vehicles within controlled airspace. In particular, as some missions involve close proximity formation flights, multi-vehicle interaction and co-operation are some of the key issues that need addressing. A detailed understanding of the aerodynamic coupling due to the wake induced effects of one vehicle upon another is required if excessive structural and control

loads are to be avoided.

A great deal of work has been carried out in analysing and modelling wake vortex motion and decay [1]. In some cases, interactions are avoided, such as airport operations where a minimum safety distance needs to be observed during two consecutive take-offs or landings, or in the case of air to air refuelling, where the receiver keeps clear of the wake of the tanker. However, in other cases, optimally spaced vehicles benefit from favourable wake vortex induced interactions [2, 3, 4, 5, 6], similar to that used by geese when flying in formation [7]. These benefits include reduced induced drag for the trailing aircraft, which translates into significant fuel savings and/or increased range with a given payload. Flight tests performed at the NASA Dryden Flight Research Center as part of the Autonomous Formation Flight programme (AFF) demonstrated up to 18% reduction in fuel consumption [8, 9, 10].

With the current and growing need for new technologies to lower fuel costs, and for new Air Traffic Control (ATC) procedures to increase the capacity of an already busy airspace without compromising safety [11], realistic models of aerodynamic coupling between air-vehicles in close proximity need to be developed and the risks and issues associated with wake vortex evolution and encounter need to be assessed. Previous techniques [12] used to model vortex-induced effects can be divided in two main categories: (i) theoretical and experimental methods using look-up databases (from CFD models [13, 14], wind tunnel and/or flight test measurements [15]); (ii) computational methods [16]. The latter include, from the simplest to the most involved: Prandtl's lifting line theory (single horseshoe vortex) [17, 18, 19, 20, 21, 22]; Vortex Lattice Methods (VLM) with or without viscous core [23, 24, 25]; improved methods taking account of the roll-up of the wake [7, 26, 27, 28, 29].

Furthermore, to assess the influence of these aerodynamic cross-coupling effects on the control systems and operating procedures, the models need to be incorporated into real-time simulation environments [30, 31]. Look-up database approaches present a double disadvantage: not only are they extremely computationally demanding to handle in real-time, but these databases can only be used for a specified air-vehicle and a range of flight conditions [32]. Simple computational methods are rapid, but the results are not always realistic or accurate enough. However, with increasing accuracy comes increasing computation time. Hence choosing a computational method to model the wake vortex involves finding a compromise between accuracy and rapidity of execution.

This paper describes the development of a computational method and simulation models that incorporate wake vortex effects associated with air vehicles flying in close proximity. The aim has been to develop a generic wake vortex model which could be used for any type of wing geometry, and still produce results which could be used in a real-time Synthetic Environment. Using the same VLM to model both vehicles has allowed them to exchange position during simulations. The non-uniform vortex-induced wind and wind gradients acting on the trail aircraft have been approximated as effective wind and wind gradients and directly used within dynamic simulations, following the method developed by Dogan and colleagues [32, 33, 34, 35, 36, 37, 38, 39].

In the following sections, first the WVM, then the model integration process are described, followed by some results and conclusions, and an outlook on further developments.

Wake Vortex Model

A one-lifting-line vortex lattice method for linear aerodynamic wing applications has been developed and implemented in MATLAB. The code (ELL) computes the steady-state velocity induced by the wake of one or more air-vehicles at a given location using Weissinger's extended lifting-line theory [40, 41], and supports 3D, subsonic multi-wing designs with swept, tapered, twisted wings of any aspect ratio, with or without dihedral.

Special care was used to maintain the symmetry between the leading and following air-vehicles in order to allow them to exchange positions during simulations. As a consequence, the modelling reference frame could not be attached to any particular air-vehicle. Hence, it was decided to work in the inertial NED (North East Down) frame: not only was this reference frame independent of UAV positions and orientations, but it presented advantages when interfacing the simulation with visualisation tools such as FlightGear [42, 43] or AVDS [44, 45].

(i) Modelling of the wing

Each air-vehicle is represented by its lifting surfaces. The vortex generating surface is replaced by its 1/4-chord segment, and the vortex sheet by a flat rectangular surface composed of n_{seg}

semi-infinite horseshoe vortices. These are attached to the 1/4-chord line, follow the chord up to the 3/4-chord line, and extend downstream to infinity in parallel with the aircraft velocity vector **V** (cf. Fig. 1). The filled circles in Fig. 2 represent the

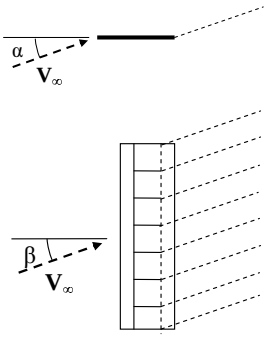


Figure 1: Vortex sheet positioning

control points where the boundary conditions are met, and the enlarged panel in Fig. 3 shows how the horseshoe vortex is positioned. Figure 4 illustrates

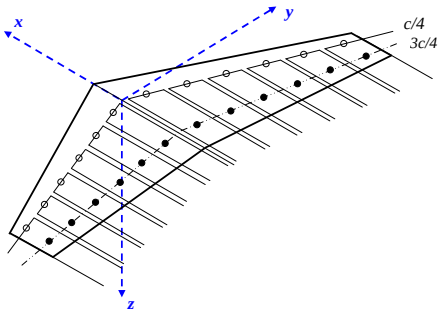


Figure 2: Modelling of the wing

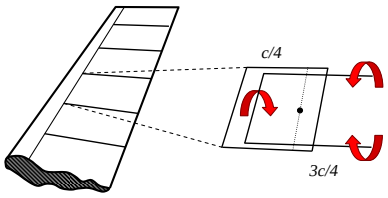


Figure 3: Horseshoe vortex positioning

the geometry of a basic air-vehicle (main wing, fin and tailplane are represented), and the vortex layout of the corresponding vehicle for $\alpha = 5°$.

(ii) Calculation of the vorticity vector

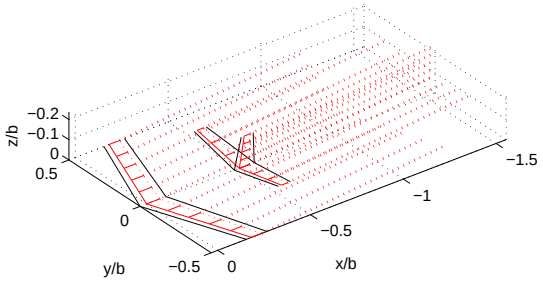


Figure 4: 3D wing configuration and vortex layout

The circulation along each horseshoe vortex is assumed to be constant. The problem formulation described herein leads to an integro-differential equation for the unknown circulation distribution. It is solved using Weissinger's boundary condition [40]: at the control points, the intensity of the vortex filaments must be such that the airflow is tangential to the wing surface:

$$(\mathbf{V_i} + \mathbf{V}).\mathbf{n} = 0 \qquad (1)$$

(iii) Calculation of the induced velocity field

Each horseshoe vortex is composed of 5 straight branches, as shown in Fig. 5. Branch 1 is bound to the 1/4-chord line of the wake generating surface; from there, branches 2 and 3 follow the chord up to the 3/4-chord line; finally, branches 4 and 5 extend downstream to infinity, parallel with the upstream velocity vector. The vortex shape was adapted to prevent any singularity due to an infinitely thin filament where all the vortex strength would be concentrated. A viscous core and time decay effect were added to the semi-infinite downstream branches (branches 4 and 5) of each vortex. A Kurylowich model [46] was used to represent the vorticity of these branches as a Gaussian distribution of standard deviation $r_c/\sqrt{2}$, where r_c is the core radius of the vortex branch.

Once the circulation distribution is known, the velocity induced by the wake-generating vehicle(s) can be calculated at any field point $P(x_P, y_P, z_P)$, using the Biot-Savart law ([12], p. 400). The contribution of each branch $j \in [1, 5]$ of the horseshoe vortex $k \in [1, n_{seg}]$, of strength Γ_k, to the induced velocity

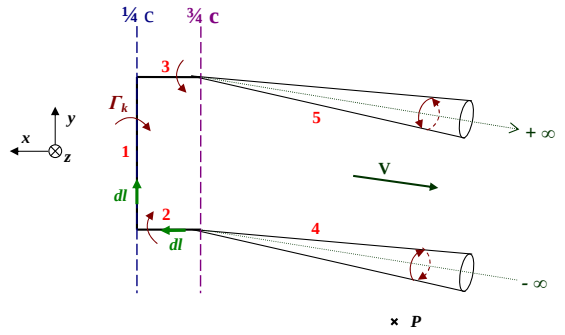


Figure 5: Schematic of an adapted horseshoe vortex (straight wing)

$\mathbf{Vi_k}$ at the point $P(x_P, y_P, z_P)$ is given by (cf. Fig. 6):

$$\mathbf{Vi_{k,j}}(x_P, y_P, z_P) = \frac{\Gamma_k}{4\pi} \int_{\theta_{k,j}=\gamma_{k,j}}^{\theta_{k,j}=\delta_{k,j}} \frac{\mathbf{dl_{k,j}} \wedge \mathbf{r_{k,j}}}{\|\mathbf{r_{k,j}}\|^3} \qquad (2)$$

where $\gamma_{k,j}$ and $\delta_{k,j}$ are illustrated in Fig. 7. In the case of the semi-infinite branches 4 and 5, then $\gamma_{k,4} = 0$ and $\delta_{k,5} = \pi$.

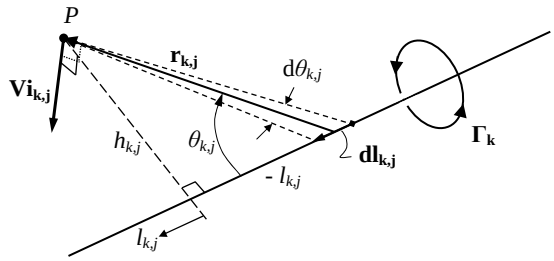


Figure 6: 3D straight vortex - Branch j of the horseshoe vortex k

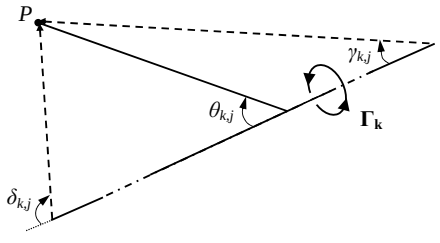


Figure 7: Integration angles - Branch j of the horseshoe vortex k

As the vortex branches are straight, Eq. 2 leads to:

$$\mathbf{Vi_{k,j}} = \frac{\Gamma_k}{4\pi h_{k,j}} [\mathrm{Cos}(\gamma_{k,j}) - \mathrm{Cos}(\delta_{k,j})] . \Upsilon_{k,j} . \mathbf{n_{k,j}} \qquad (3)$$

where $\mathbf{n_{k,j}}$ is the unit vector in the normal direction, and $\Upsilon_{k,j}$ represents the decay of the vortex strength. For the branches bound to the wing ($j \in \{1, 2, 3\}$), the vortex strength remains constant:

$$\Upsilon_{k,j} = 1 \qquad (4)$$

For the trailing branches ($j \in \{4, 5\}$), the decay is applied uniformly along their entire length and is defined as [46]:

$$\Upsilon_{k,j} = 1 - e^{-1.26(h_{k,j}/r_{c_{k,j}})^2} \qquad (5)$$

where $h_{k,j}$ is the perpendicular distance of the field point from the branch line j, $r_c = 2.24\sqrt{\nu\tau_{k,j}}$ is the core radius of the vortex branch j [38], ν is the kinematic viscosity of the air, and $\tau_{k,j}$ is the age of the vortex branch (defined as the distance from the vortex origin (on the 1/4-chord line of the wing), divided by the airspeed V).

The velocity induced at P by the horseshoe vortex k is equal to the sum of the contributions of its 5 branches:

$$\mathbf{Vi_k}(x_P, y_P, z_P) = \sum_{j=1}^{5} \mathbf{Vi_{k,j}}(x_P, y_P, z_P) \qquad (6)$$

The total induced velocity at $P(x_P, y_P, z_P)$ is then obtained by adding the velocities induced by each of the n_{seg} horseshoe vortices used to model the lifting surfaces of the wake-generating vehicle:

$$\mathbf{Vi}(x_P, y_P, z_P) = \sum_{k=1}^{n_{seg}} \mathbf{Vi_k}(x_P, y_P, z_P) \qquad (7)$$

Figure 8 shows the induced velocity field in the yz-plane at different values of x behind a rectangular wing ($\alpha = 5$ deg). The usual shape of wing-tip vortices can be clearly seen: downwash inboard of the wing-tip, and upwash outboard of it. Furthermore, the decay effect is easily observed, as the vortex core gets larger and its strength weaker when the yz-plane moves downstream. Finally, it should be noted that body axes were used to plot the induced velocity field, whence the seemingly upward movement of the trailing vortices.

(iv) Induced wind velocity and body angular rates

If N vehicles are flying in close proximity, the velocity induced on the vehicle k by the surrounding air-vehicles $j \neq k$ is computed at each of the n_{seg_k}

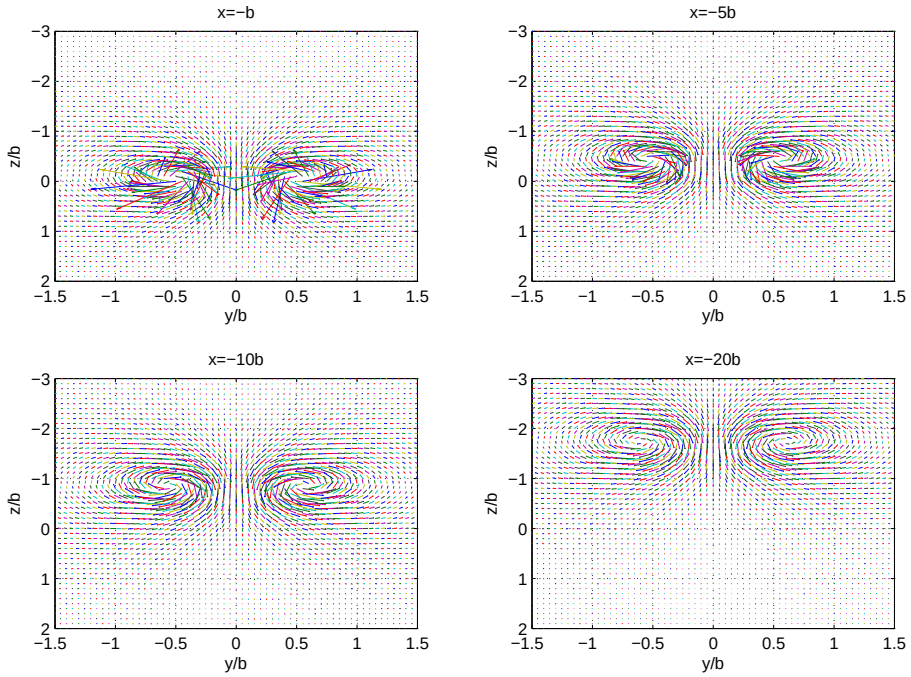


Figure 8: Slice views of the induced velocity field in the *yz*-plane behind a rectangular wing in its body axes ($\alpha = 5$ deg)

calculation point (along the 1/4-chord line) of the vehicle k using Eq. 7. The induced velocity field thus obtained is highly non-uniform, and can be approximated around the centre of gravity of vehicle k as the sum of uniform wind components and uniform wind gradients:

$$\mathbf{Vi}(G_k) = \begin{pmatrix} \widetilde{Vi_x} + \frac{\widetilde{\partial Vi_x}}{\partial x} + \frac{\widetilde{\partial Vi_x}}{\partial y} + \frac{\widetilde{\partial Vi_x}}{\partial z} \\ \widetilde{Vi_y} + \frac{\widetilde{\partial Vi_y}}{\partial x} + \frac{\widetilde{\partial Vi_y}}{\partial y} + \frac{\widetilde{\partial Vi_y}}{\partial z} \\ \widetilde{Vi_z} + \frac{\widetilde{\partial Vi_z}}{\partial x} + \frac{\widetilde{\partial Vi_z}}{\partial y} + \frac{\widetilde{\partial Vi_z}}{\partial z} \end{pmatrix} \tag{8}$$

where:

$$\begin{cases} \widetilde{Vi_x} = \dfrac{1}{n_{seg_k}} \displaystyle\sum_{j=1}^{n_{seg_k}} Vi_{x_j} \\ \widetilde{Vi_y} = \dfrac{1}{n_{seg_k}} \displaystyle\sum_{j=1}^{n_{seg_k}} Vi_{y_j} \\ \widetilde{Vi_z} = \dfrac{1}{n_{seg_k}} \displaystyle\sum_{j=1}^{n_{seg_k}} Vi_{z_j} \end{cases} \tag{9}$$

and:

$$\begin{cases} \dfrac{\widetilde{\partial Vi_x}}{\partial y} = \dfrac{1}{n_{seg_k}-1} \displaystyle\sum_{j=1}^{n_{seg_k}-1} \frac{Vi_{x_{j+1}} - Vi_{x_j}}{y_{j+1} - y_j} \\ \dfrac{\widetilde{\partial Vi_y}}{\partial y} = \dfrac{1}{n_{seg_k}-1} \displaystyle\sum_{j=1}^{n_{seg_k}-1} \frac{Vi_{y_{j+1}} - Vi_{y_j}}{y_{j+1} - y_j} \\ \dfrac{\widetilde{\partial Vi_z}}{\partial y} = \dfrac{1}{n_{seg_k}-1} \displaystyle\sum_{j=1}^{n_{seg_k}-1} \frac{Vi_{z_{j+1}} - Vi_{z_j}}{y_{j+1} - y_j} \end{cases} \tag{10}$$

The components of the effective induced translational wind velocity vector $\widetilde{\mathbf{Vi}}$ are directly defined as $\widetilde{Vi_x}$, $\widetilde{Vi_y}$ and $\widetilde{Vi_z}$, and the components of the effective induced rotational wind velocity vector $\widetilde{\boldsymbol{\omega}_i}$ are derived from the uniform wind gradients using:

$$\begin{cases} \widetilde{\omega i_x} = \dfrac{\widetilde{\partial Vi_z}}{\partial y} - \dfrac{\widetilde{\partial Vi_y}}{\partial z} \\ \widetilde{\omega i_y} = \dfrac{\widetilde{\partial Vi_x}}{\partial z} - \dfrac{\widetilde{\partial Vi_z}}{\partial x} \\ \widetilde{\omega i_z} = \dfrac{\widetilde{\partial Vi_y}}{\partial x} - \dfrac{\widetilde{\partial Vi_x}}{\partial y} \end{cases} \tag{11}$$

NB: These partial derivatives are approximated us-

ing the averages along the spanwise axis of the wing, therefore the dx and dz terms are very small for most wing configurations (low sweep and low dihedral angles). When this is the case, the corresponding derivatives can then be reasonably neglected.

(v) Limitations of the model

ELL is based on a small-perturbation potential flow theory, therefore reliable results can only be achieved for small angles of attack and subsonic conditions.

The model does not allow the following effects to be taken into account: thickness, camber, fuselage, friction drag, and compressibility; the roll-up of the vortex sheet is also ignored.

Finally, as the calculation points distribution of a wing is collapsed to a single line along its 1/4-chord line, the wake-induced pitching moment cannot be accurately calculated. A way to improve these results would be to use more calculation points for the estimation of the induced velocity field on the receiving wing, and to locate these points at different values of x (i.e. chordwise), and of z (i.e. above and below the wing). However, adding calculation points would lead to an increased computational time and slow down the simulations.

Model Integration Process

This section briefly explains how the WVM can be integrated into Simulink simulations.

To enable the air-vehicles to exchange positions, the whole integration scheme needs to be symmetric. Consequently, the dynamics of all UAVs in the formation need to be modified to take account of the effects induced by the wakes of the others. Figure 9 shows how the WVM has been integrated in a two-vehicle-formation flight simulation: the state parameters of each vehicle, such as their positions (x, y, z), their orientations (Euler angles: ϕ, θ, ψ) in a common North-East-Down inertial reference frame, and their respective airdata (V, α, β) are sent to the s-function block "ELLmain" which calls the main MATLAB function of the airwake model, `ELLmain.m`. `ELLmain.m` calculates the effective wind velocities induced on each vehicle by its neighbour(s), and feeds them back into the wind terms of the vehicle dynamics, as shown in Fig. 10.

The induced airspeed and body angular rates can then be calculated for each wake-encountering vehicle using the following equations:

$$\begin{cases} V_{x_\Delta} = -\widetilde{Vi_x} \\ V_{y_\Delta} = -\widetilde{Vi_y} \\ V_{z_\Delta} = -\widetilde{Vi_z} \end{cases} \tag{12}$$

and:

$$\begin{cases} p_\Delta = -\widetilde{\omega i_x} \\ q_\Delta = -\widetilde{\omega i_y} \\ r_\Delta = -\widetilde{\omega i_z} \end{cases} \tag{13}$$

As described in Venkataramanan and Dogan's work [33, 35, 36, 38], the main advantage of using this method is that it removes the need to explicitly compute the forces and moments induced by one vehicle in the equations of motion of the others. It is therefore more computationally efficient.

The WVM was successfully implemented within the Cranfield University Air-Vehicle Simulation and Visualisation Environment, and within the Cobham Synthetic Environment that has been developed as part of the ASTRAEA programme [47].

Results and Observations

This section presents the computational results obtained with ELL for two vehicles flying in close formation flight at $V = 19.8171$ m/s, $\alpha = 8$ deg, and $\beta = 0$ deg. The results are compared to wind-tunnel measurements [5], to predictions from the planar vortex lattice method HASC95 (with 540 panels used to model each aircraft: 36 in the spanwise direction and 15 in the chordwise direction) [5], and to computational results obtained by Dogan using a modified Horseshoe Vortex Model (HVM) [38]. The effects of the wake generated by the upstream vehicle (referred to as the leader or UAV_1) upon the downstream vehicle (referred to as the follower or UAV_2) are analysed.

(i) Test configuration and preliminary observations

The test vehicles are two 1/13-scale Lockheed tailless aircraft models consisting of a 65 deg delta wing with a sawtooth trailing edge with sweep angles of 25 deg. For the wind-tunnel test, the inlets were blocked and both models were mounted in close proximity at an angle of attack of 8 deg relative to the freestream. The test configuration is illustrated in Fig. 11.

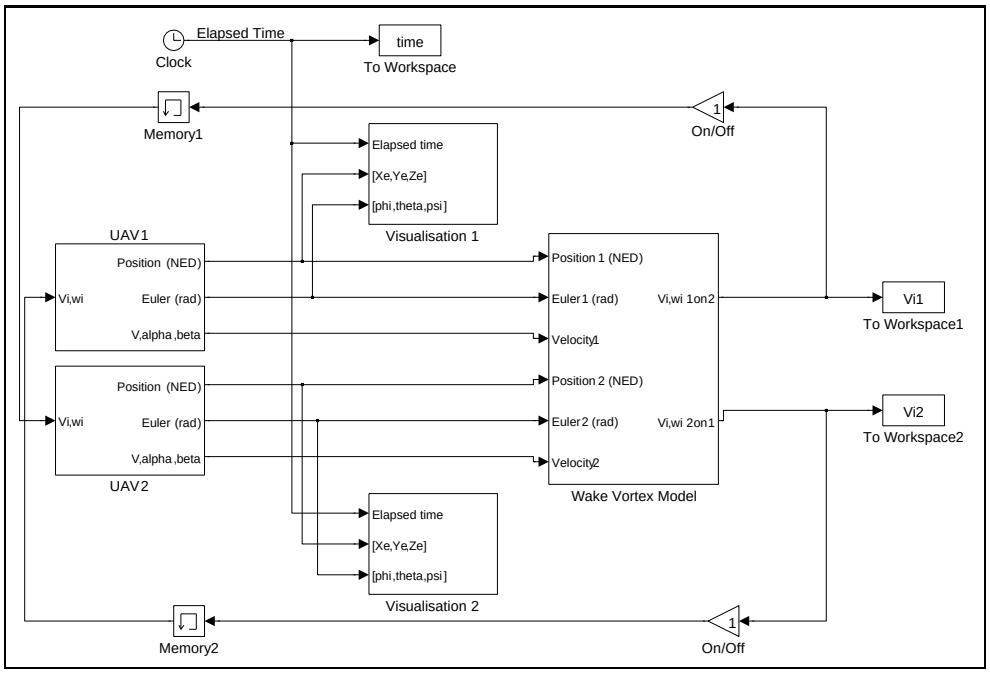


Figure 9: Simulink Simulation Model

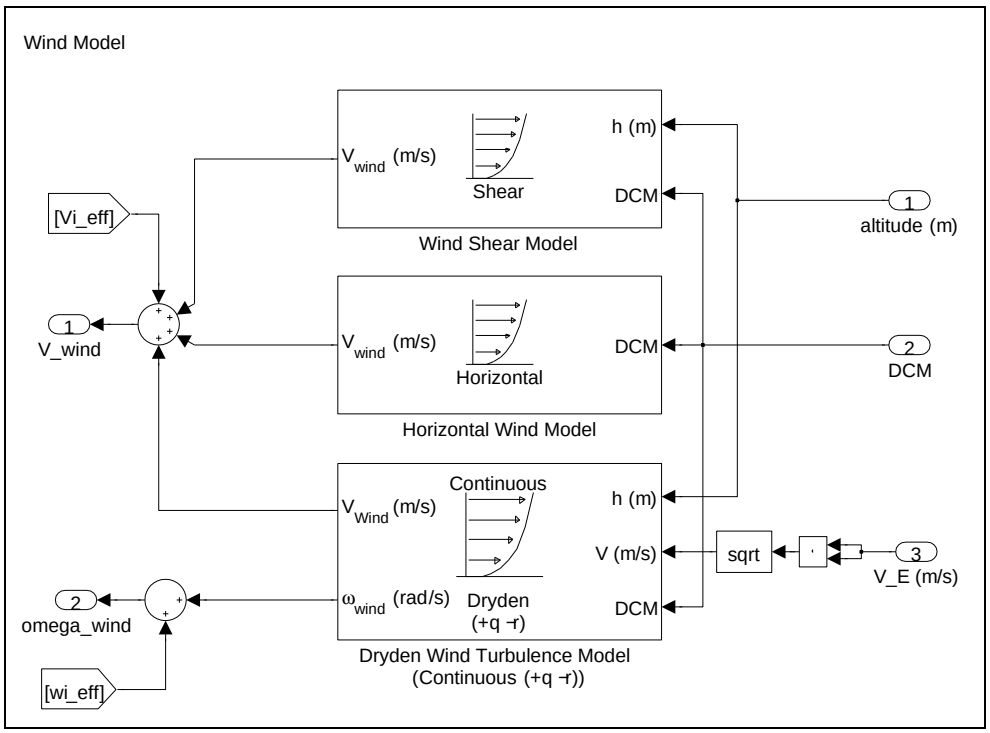


Figure 10: UAV Wind Model

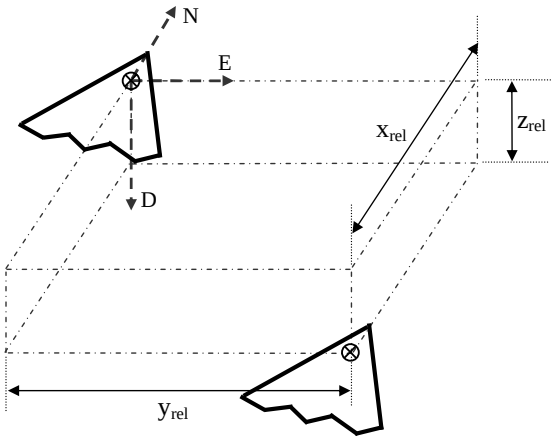


Figure 11: Test configuration

The geometric parameters for both wings, as used in ELL, are as follows: number of horseshoe vortices per wing: $n_{seg} = 10$; wing span: b = 0.8796 m; aspect ratio: $\lambda = 1.7394$; taper ratio: $\varepsilon = 0$; sweep angle of the 1/4-chord line: $\varphi = 58$ deg; dihedral angle: $\delta = 0$ deg; twist angle (washout): $+ve = 0$ deg.

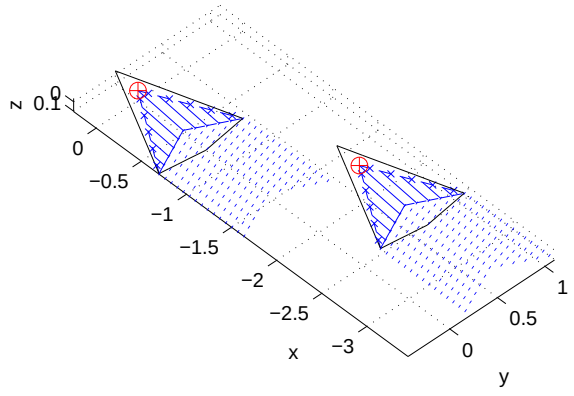


Figure 12: ELL: air-vehicle geometry and vortex layout

As can be seen from Fig. 12, the UAVs saw-tooth trailing edges cannot be properly modelled with ELL (due to the use of only one chordwise panel), and are therefore represented with a straight line.

HASC95 uses a flat wake approximation, i.e., the trailing legs of the horseshoe vortices extend downstream to infinity, parallel to the *xy* body plane, and do not vary with the angle of attack. In comparison, both Dogan's model and ELL represent the trailing legs of the horseshoe vortices as extending downstream to infinity, parallel to the freestream direction. The difference between Dogan's model and ELL mainly comes from the number of horseshoe vortices used to model the wing: Dogan uses only one horseshoe vortex, which only allows basic wing planforms to be represented, whereas ELL uses a variable number of horseshoe vortices, which allows a more accurate representation of the wing geometry. Typically, Dogan's model is only valid for untapered wings and the 65 deg delta wings used for wind tunnel testing were approximated as untapered 30-deg wings. Besides, Dogan's horseshoe vortex is a 3-leg horseshoe vortex, whose trailing legs separate from the wing surface at the 1/4-chord line (i.e. where the bound vortex is attached to the wing), whereas ELL's horseshoe vortices follow the wing surface chordwise up to the 3/4-chord line before separating to extend downstream to infinity.

Another difference worth noting between Dogan's method and ELL concerns the modelling of the following UAV. Dogan uses a stick diagram composed of 4 sticks to represent the aircraft body: one along the *x* body axis representing the fuselage length, one along the *z* body axis representing the fuselage height, and finally two sticks representing each wing (with dihedral and swept angles). In comparison, ELL uses the same wing discretisation model for all UAVs. As already mentioned, the motivation behind this choice is to facilitate the simulation of reconfiguration scenarios where each vehicle may have to fulfill both wake-generating and wake-encountering functions, depending on its position in the formation.

(ii) Effective induced wind velocities

The variations with lateral spacing of the incremental translational and rotational wind velocities induced by UAV_1 on UAV_2 are shown in Figs 13 and 14 respectively. They are compared to Dogan's modified HVM results [38]. As $\beta = 0$ deg, all plots are perfectly symmetric against *y*. The peak value of $\widetilde{Vi_z}$ is obtained when UAV_2 is lined up behind UAV_1: that is when the downwash originated from each wing-tip vortex combines with the same maximum intensity. At this point, it can be noticed that the effects of the wing-tip vortices on $\widetilde{Vi_y}$ are cancelling each other, as are the effects of the wing-tip vortices on the effective induced rotational wind velocities $\widetilde{\omega i_x}$ and $\widetilde{\omega i_z}$.

The difference between Dogan's modified HVM and ELL comes from the fact that Dogan's horse-

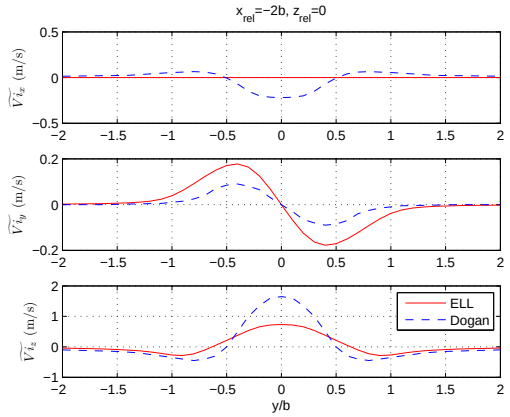


Figure 13: Variations of the effective induced translational wind velocity components with lateral spacing

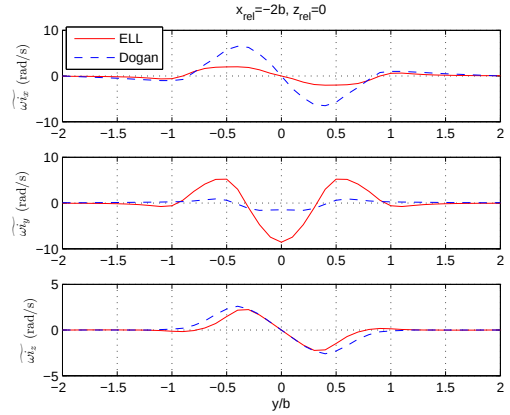


Figure 14: Variations of the effective induced rotational wind velocity components with lateral spacing

shoe vortices separate from the wing surface at its 1/4-chord line, whereas with ELL, the separation occurs at the wing 3/4-chord line. As a consequence, the vortices are positioned higher relatively to UAV_2 in Dogan's case than in our case. UAV_2 moves along the $z = 0$ line, which, in Dogan's case, corresponds to the centre-line of the vortex, whence the higher upwash and downwash experienced. In our case, the $z = 0$ line crosses the vortex in its upper part, where the sidewash is stronger. Also, a difference is to be noted in the forward-wash. This is due to the fact that in Dogan's case, the effects of UAV_1 upon UAV_2 are integrated over UAV_2's whole body length, whereas in our case they are only integrated along the 1/4-chord line of its wings. As a consequence, the overall offset between UAV_2 and UAV_1's 1/4-chord line bound vortex (responsible for the forward/backward-wash) is higher in Dogan's case than in our case, thereby inducing a stronger forward-wash effect.

The variations with longitudinal spacing of the incremental translational and rotational wind velocities induced by UAV_1 on UAV_2 are shown in Figs 15 and 16 respectively. UAV_2 being situated starboard ($y_{rel} \geq 0$) and below ($z_{rel} \geq 0$) UAV_1, it is – as expected – subjected to starboard sidewash ($\widetilde{Vi_y} \geq 0$) and upwash ($\widetilde{Vi_z} \leq 0$). The presence of the vortex decay can be seen from the fact that all the induced velocities tend to zero when the longitudinal distance between UAV_1 and UAV_2 increases.

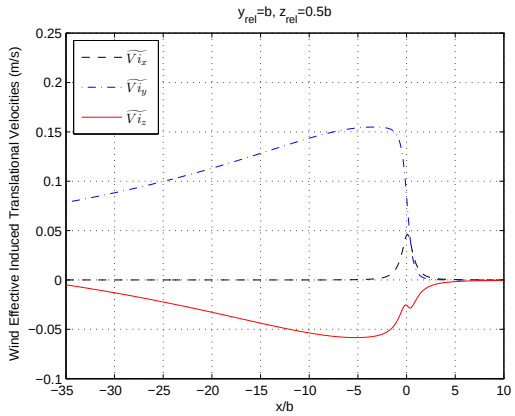


Figure 15: Variations of the effective induced translational wind velocity components with longitudinal spacing

The "bumps" in $\widetilde{Vi_x}$ and $\widetilde{Vi_z}$ around $x/b = 0$ are due to the effects of UAV_1's 1/4-chord line bound

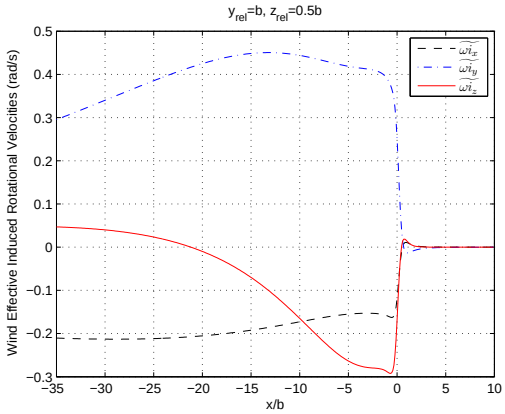


Figure 16: Variations of the effective induced rotational wind velocity components with lateral spacing

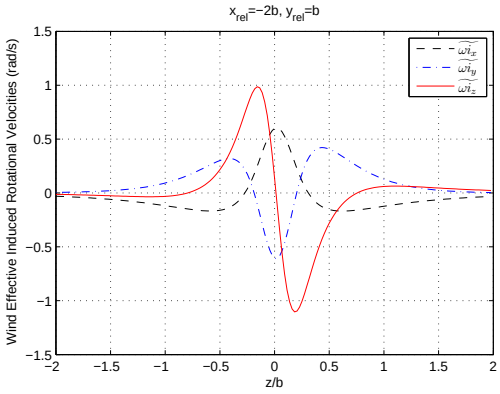


Figure 18: Variations of the effective induced rotational wind velocity components with vertical spacing

vortex as UAV_2 passes just above it. Finally, $x \geq 0$ corresponds to UAV_2 being in front of UAV_1, where it is subjected to almost no influence from UAV_1.

The variations with vertical spacing of the incremental translational and rotational wind velocities induced by UAV_1 on UAV_2 are shown in Figs 17 and 18 respectively. The follower is situated starboard ($y_{rel} \geq 0$) and behind ($x_{rel} \leq 0$) the leader. Consequently, it is subjected to port sidewash ($\widetilde{Vi_y} \leq 0$) when above the wake, to starboard sidewash ($\widetilde{Vi_y} \geq 0$) when below the wake, and to upwash ($\widetilde{Vi_z} \leq 0$) when near the wake ($z \simeq 0$).

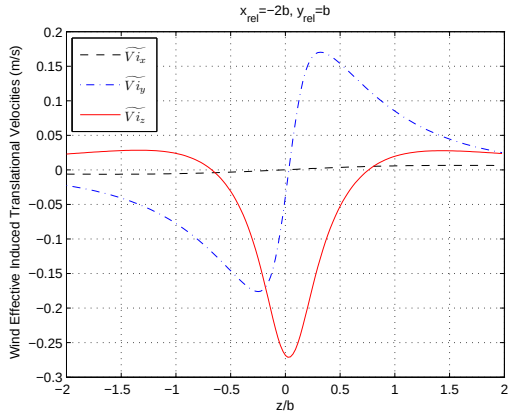


Figure 17: Variations of the effective induced translational wind velocity components with vertical spacing

The slight asymmetry between $z/b \leq 0$ and $z/b \geq 0$ and the reason why the plots look slightly shifted towards $z/b \leq 0$ is because the wake vortex sheet is not symmetric against z. This is due to the fact that it separates from UAV_1 at its 3/4-chord, which, for $\alpha = 8$ deg, is situated below the line $z = 0$, i.e. at $z \geq 0$). The peak value of $\widetilde{Vi_z}$ is obtained when UAV_2 is at the same level as UAV_1's wake vortex sheet. That is also when the peak value of $\widetilde{Vi_x}$ is reached and when $Vi_y(z)$ suddenly changes direction, leading to a steep change of sign in $\widetilde{Vi_y}$ and a peak in $\widetilde{\omega i_y}$.

(iii) Incremental forces and moments coefficients

As literature data sets are usually provided in terms of induced forces and moments coefficients, these were computed from the induced velocity field obtained with ELL (using the Kutta-Joukowski theorem), and compared to wind tunnel tests measurements [5], HASC95 computational results [5], and Dogan's results [38].

The variations of the incremental lift coefficient with lateral and vertical spacing are shown in Figs 19 and 20 respectively. On both plots, ELL results are very close to HASC95 results, with HASC95 using 540 calculation panels on each vehicle and ELL using only 10.

From Fig. 19, it can be seen that the maximum lift loss is encountered when UAV_2 is positioned directly behind UAV_1, i.e. when the induced downwash is maximum. As UAV_2 moves sideways, the downwash intensity decreases (i.e. the incremental lift coefficient increases), and upwash is encountered as UAV_2 passes UAV_1's wing tip. The maximum upwash is

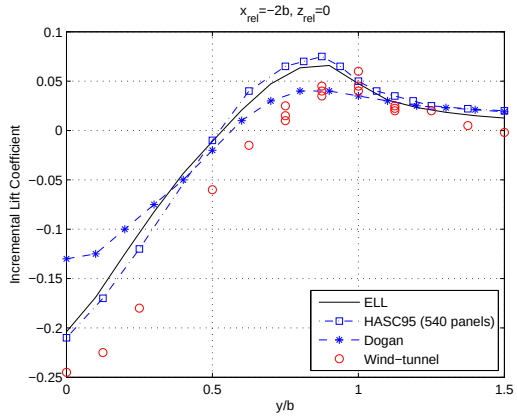


Figure 19: Variations of the incremental lift coefficient with lateral spacing

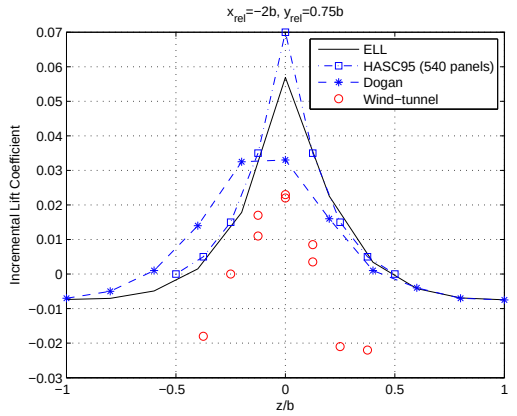


Figure 20: Variations of the incremental lift coefficient with vertical spacing

encountered at $y \simeq 0.8b$, which is consistent with the optimum lateral spacing for formation flight [4]. As UAV_2 keeps on moving outboard of UAV_1, the effect fades away and the incremental lift coefficient tends to zero.

Fig. 20 represents the vertical variations of the wake-induced lift coefficient for $y = 0.75b$, i.e for a lateral spacing close to the optimal one. It shows a maximum upwash for $z = 0$, i.e. when UAV_2 is aligned behind UAV_1, which is also consistent with the "sweet spot" position [4]. The maximum wake-induced lift increment is over-estimated, but the trend is well predicted.

The variations of the incremental drag coefficient with lateral and vertical spacing are shown in Figs 21 and 22 respectively.

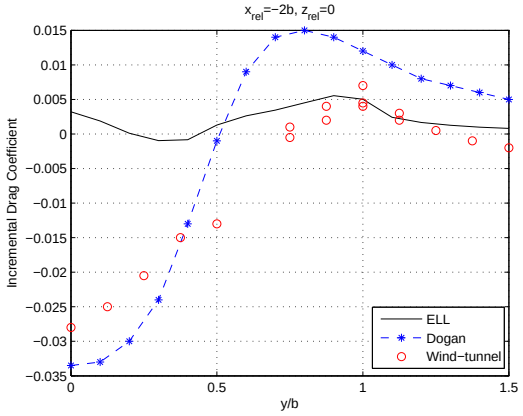


Figure 21: Variations of the incremental drag coefficient with lateral spacing

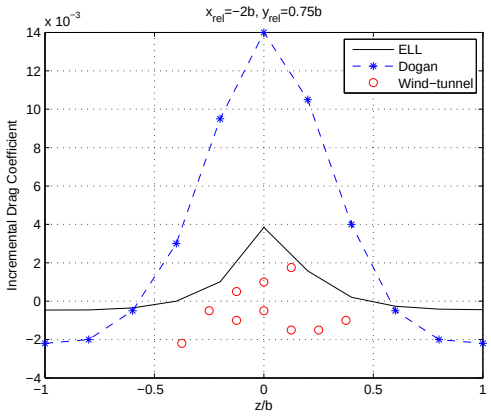


Figure 22: Variations of the incremental drag coefficient with vertical spacing

As can be seen from Fig. 21, the predictions only match the data for $y/b \geq 0.75$. It is to be noted that the drag increment calculated by ELL takes account of the induced drag only, whereas the wind-tunnel measurements also include the profile drag.

The variations of the wake-induced drag increment with vertical spacing (see Fig. 22) show a better match with the wind-tunnel measurements. The peak at $z/b = 0$ is a consequence of the peak in incremental lift shown in Fig. 20.

The variations of the incremental rolling moment coefficient with lateral and vertical spacing are shown in Figs 23 and 24 respectively. The induced rolling moment being the largest vortex-induced effect and the most critical for flight safety, it is quite important that it is well-predicted.

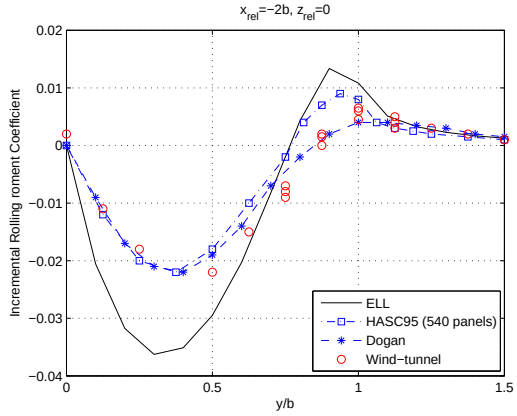


Figure 23: Variations of the incremental rolling moment coefficient with lateral spacing

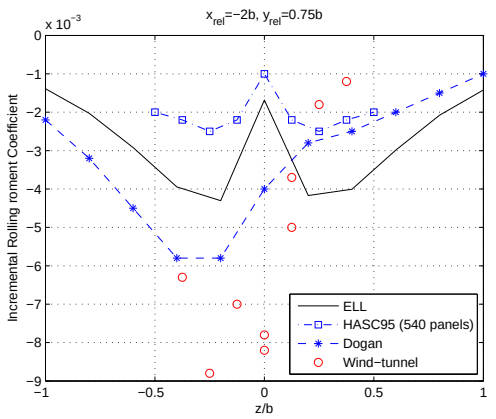


Figure 24: Variations of the incremental rolling moment coefficient with vertical spacing

As can be seen from Fig. 23, the trend of its variations with lateral spacing is very well predicted, although the peak magnitude is over-estimated. According to Blake [5], a maximum (30 deg) elevon deflection gives a rolling moment increment of -0.022, so the effect of UAV_1 upon UAV_2 is similar to – or greater than – a full control deflection. This result confirms the importance of wake-induced effects in close formation flight and the necessity to include them within simulation models.

The variations with vertical spacing (see Fig. 24) seem to be a middle ground between the results obtained with HASC95 and those obtained by Dogan with his modified HMV. The trend does not match the wind-tunnel measurements very well, but considering that the amplitude of the variations with vertical spacing are about 10 times smaller than with lateral spacing, that should not be a significant problem.

ELL results compared satisfactorily with the published data. It is to be noted that the aim of ELL is not to get a perfect match, but to obtain a match which is good enough to predict the qualitative, and to some extent, the quantitative effects of aerodynamic interactions between air-vehicles flying in close proximity, using a fast and efficient method.

(iv) Computational time

For 2 UAVs, the total time taken by an Intel(R) Xeon(R) CPU E5410 @ 2.33GHz, 2.00GB of RAM to model the wings and to compute the induced velocity field generated by the leader upon the follower, is: $\simeq$ 0.015 s for 4 discretisation segments per wing; $\simeq$ 0.029 s for 6 discretisation segments per wing; $\simeq$ 0.072 s for 10 discretisation segments per wing. Consequently the rapidity of execution is sufficient for the model to be used in near real-time simulations.

Conclusions

ELL is a novel WVM which has been developed in order to assess the aerodynamic coupling between air-vehicles flying in close formation. It is sufficiently representative to support studies of aerodynamic interaction between multiple air vehicles and fast enough to be used within real time or near real time air-to-air simulations.

As ELL is based on a small-perturbation potential flow theory, reliable results can only be achieved for

small angles of attack and subsonic conditions. Also, it should be noted that thickness, camber, fuselage, friction drag, and compressibility are not taken into account; nor is the roll-up of the vortex sheet. Finally, as the control points of a wake-encountering wing are all situated along its 1/4-chord line, the pitching moment induced by the wake-generating air-vehicle(s) cannot be accurately calculated

ELL was satisfactorily validated, and successfully integrated within Simulink air-vehicle simulations using a method developed by Dogan [32, 33, 34, 35, 36, 37, 38, 39]: the nonuniform induced velocity field was approximated as uniform wind components and gradients, and used directly in the equations of motion of the following vehicle via its wind terms. Compared to previous work carried out in this field, the modelling and integration technique presented in this paper enables the lead and trail air-vehicles to exchange positions during the simulations.

Further Developments

Further developments will include testing the model for more complex flight paths, and use the simulation models to support an in-depth investigation into the nature of dynamic air vehicle coupling and the likely impact on autonomous control requirements for multiple vehicle deployment. In particular, different reconfiguration scenarios will be studied.

Acknowledgements

This research was conducted in collaboration with Cobham plc and funded by the Technology Strategy Board within the ASTRAEA programmes's Multiple Air Vehicle Integration Project (TP/3/DSM/6/I/15769). The preliminary version of ELL was based on a model developed by Clement Toussaint from Onera, France.

References

[1] Greene, G.C. An approximate model of vortex decay in the atmosphere. *Journal of Aircraft*, 1986, **23**, pp 566-573.

[2] Blake, W and Multhopp, D. Design, performance and modeling considerations for close formation flight. In *AIAA Atmospheric Flight Mechanics Conference and Exhibit*, AAIA 98-4343, Boston, MA, Aug. 10-12 1998.

[3] Myatt, J.H. and Blake, W.B. Aerodynamic database issues for modeling close formation flight. In *AIAA Modeling and Simulation Technologies Conference*, AAIA 99-4194, Portland, OR, Aug. 9-11 1999.

[4] Blake, W.B. An aerodynamic model for simulation of close formation flight. In *AIAA Modeling and Simulation Technologies Conference and Exhibit*, AAIA 2000-4304, Denver, CO, Aug. 14-17 2000.

[5] Blake, W.B. and Gingras, D.R. Comparison of predicted and measured formation flight interference effects. *Journal of Aircraft*, Mar.-Apr. 2004, **41**, (2), pp 201-207.

[6] Blake, W.B., Dickes, E.G. and Gingras, D.R.. UAV aerial refueling - wind tunnel results and comparison with analytical predictions. In *AIAA Atmospheric Flight Mechanics Conference and Exhibit*, AAIA 2004-4820, Providence, RI, Aug. 16-19 2004.

[7] Beukenberg, M and Hummel, D. Aerodynamics, performance and control of airplanes in formation flight. In *Proceedings of the 17th Congress of ICAS*, volume 2, pp 1777-1794, Stockholm, Sweden, Sept. 9-14 1990.

[8] Hansen, J.L. and Cobleigh, B.R. Induced moment effects of formation flight using two F/A-18 aircraft. In *AIAA Atmospheric Flight Mechanics Conference and Exhibit*, AIAA 2002-4489, Monterey, CA, Aug. 5-8 2002.

[9] Lavretsky, E and Misovec, K. Phase I: Formation flight control design. In *AIAA's 1st Technical Conference and Workshop on Unmanned Aerospace Vehicles*, 2002.

[10] Vachon, M.J., Ray, R.J., Walsh, K.R. and Ennix, K. F/A–18 aircraft performance benefits measured during the autonomous formation flight project. In *AIAA Flight Mechanics Conference and Exhibit*, AIAA 2002-4491, Monterey, CA, Aug. 5-8 2002.

[11] Proctor, F.H. and Switzer, G.F. Numerical simulation of aircraft trailing vortices. In *9th Conference on Aviation, Range and Aerospace Meteorology*, pp 511-516, 2000.

[12] Anderson, J.D. *Fundamentals of Aerodynamics*. Boston: McGraw-Hill, fourth edition edition, 2007.

[13] Le Moigne, A and Qin, N. LES with numerical dissipation for aircraft wake vortices. In *44th AIAA Aerospace Sciences Meeting and Exhibit*, AIAA 2006-1258, Reno, NV, Jan. 9-12 2006.

[14] Spence, G.T., Le Moigne, A, Allerton, D.J. and Qin, N. Wake vortex model for real-time flight simulation based on large eddy simulation. *Journal of Aircraft*, Mar.-Apr. 2007, **44**, (2), pp 467-475.

[15] Vlachos, P and Telionis, D. Wing-tip-to-wing-tip aerodynamic interference. In *AIAA 41st Aerospace Sciences Meeting and Exhibit*, AIAA 2003-0609, Reno, NV, Jan. 6-9 2003.

[16] Margason, R.J., Kjelgaard, S.O., Sellers, W.L., Morris, C.E.K., Walkey, K.B. and Shields, E.W. Subsonic panel methods – a comparison of several production codes. In *AIAA 23rd Aerospace Sciences Meeting*, AIAA 85-0280, Reno, NV, Jan. 14-17 1985.

[17] Bloy, A.W., Lamont, P.J., Abu-Assaf, H.A. and Ali, K.A.M.. The lateral dynamic stability and control of a large receiver aircraft during air-to-air refueling. *Aeronautical Journal*, Jun.-Jul. 1986, **90**, (896), pp 237-243.

[18] Bloy, A.W., Ali, K.A.M. and Trochalidis, V. The longitudinal dynamic stability and control of a large receiver aircraft during air-to-air refueling. *Aeronautical Journal*, Feb. 1987, **91**, (902), pp 64-71.

[19] Bloy, A.W. and Trochalidis, V. The performance and longitudinal stability and control of large receiver aircraft during air to air refuelling. *Aeronautical Journal*, Dec. 1989, **93**, (930), pp 367-378.

[20] Bloy, A.W. and Trochalidis, V. The aerodynamic interference between tanker and receiver aircraft during air-to-air refueling. *Aeronautical Journal*, May 1990, **94**, (935), pp 165-171.

[21] Bloy, A.W., Trochalidis, V and West, M.G. The aerodynamic interference between a flapped tanker aircraft and a receiver aircraft during air-to-air refueling. *Aeronautical Journal*, Oct. 1991, **95**, (948), pp 274-282.

[22] Pachter, M, D'Azzo, J.J. and Proud, A.W. Tight formation flight control. *Journal of Guidance, Control, and Dynamics*, Mar.-Apr. 2001, **24**, (2), pp 246-254.

[23] Bloy, A.W., West, M.G., Lea, K.A. and Joumaa, M. Lateral aerodynamic interference between tanker and receiver in air-to-air refueling. *Journal of Aircraft*, Sept.-Oct. 1993, **30**, (5), pp 705-710.

[24] Melin, T. A vortex lattice MATLAB implementation for linear aerodynamic wing applications. Master's thesis, Royal Institute of Technology (KTH), Sweden, Dec. 2000.

[25] Karkehabadi, R. Wind-tunnel measurements of hazard posed by lift-generated wakes. *Journal of Aircraft*, Nov.-Dec. 2004, **41**, (6), pp 1424-1429.

[26] Bloy, A.W. and West, M.G. Interference between tanker wing wake with roll-up and receiver aircraft. *Journal of Aircraft*, Sept.-Oct. 1994, **31**, (5), pp 1214-1216.

[27] Bloy, A.W. and Joumaa, M. Lateral and directional stability and control in air-to-air refuelling. *Proceedings of the Institution of Mechanical Engineers Part G-Journal of Aerospace Engineering*, 1995, **209**, (G4), pp 299-305.

[28] Bloy, A.W. and Lea, K.A. Directional stability of a large receiver aircraft in air-to-air refueling. *Journal of Aircraft*, Mar.-Apr. 1995, **32**, (2), pp 453-455.

[29] Wang, Z and Mook, D.T. Numerical aerodynamic analysis of formation flight. In *41st Aerospace Sciences Meeting and Exhibit*, AAIA 2003-610, Reno, NV, Jan. 6-9 2003.

[30] Capetta, R, Giulietti, F and Innocenti, M. WakeCAD: Aerodynamics interference caculation toolbox for aircraft design, simulation and control. In *AIAA Guidance, Navigation, and Control Conference and Exhibit*, AIAA 2001-4180, Montreal, Canada, Aug. 6-9 2001.

[31] Holzapfel, F, Frech, M, Gerz, T, Tafferner, A, Hahn, K.-U., Schwarz, C, Joos, H.-D., Korn, B, Lenz, H, Luckner, R and Hohne, G. Aircraft wake vortex scenarios simulation package – WakeScene. *Aerospace Science and Technology*, 2008.

[32] Lewis, T.A. Flight data analysis and simulation of wind effects during aerial refueling. Master's thesis, The University of Texas at Arlington, 2008.

[33] Venkataramanan, S, Dogan, A, and Blake, W. Vortex effect modelling in aircraft formation flight. In *AIAA Atmospheric Flight Mechanics Conference and Exhibit*, AIAA 2003-5385, Austin, TX, Aug. 11-14 2003.

[34] Venkataramanan, S and Dogan, A. Dynamic effects of trailing vortex with turbulence & time-varying inertia in aerial refueling. In *AIAA Atmospheric Flight Mechanics Conference and Exhibit*, AIAA 2004-4945, Providence, RI, Aug. 16-19 2004.

[35] Venkataramanan, S and Dogan, A. A multi-UAV simulation for formation reconfiguration. In *AIAA Modeling and Simulation Technologies Conference and Exhibit*, AIAA 2004-4800, Providence, RI, Aug. 16-19 2004.

[36] Venkataramanan, S and Dogan, A. Modeling of aerodynamic coupling between aircraft in close proximities. In *AIAA Atmospheric Flight Mechanics Conference and Exhibit*, AIAA 2004-5172, Providence, RI, Aug. 16-19 2004.

[37] Dogan, A and Venkataramanan, S. Nonlinear control for reconfiguration of unmanned-aerial-vehicle formation. *Journal of Guidance, Control, and Dynamics*, Jul.-Aug. 2005, **28**, (4), pp 667-678.

[38] Dogan, A, Venkataramanan, S and Blake, W. Modeling of aerodynamic coupling between aircraft in close proximity. *Journal of Aircraft*, Jul.-Aug. 2005, **42**, (4), pp 941-955.

[39] Dogan, A, Sato, S and Blake, W. Flight control and simulation for aerial refueling. In *AIAA Guidance, Navigation, and Control Conference and Exhibit*, AIAA 2005-6264, San Francisco, CA, Aug. 15-18 2005.

[40] Weissinger, J. The lift distribution of swept-back wings. Technical Memorandum 1120, NACA, March 1947.

[41] Schlichting, H. *Aerodynamics of the Airplane*. McGraw-Hill, 1979.

[42] Sorton, E.F. and Hammaker, S. Simulated flight testing of an autonomous unmanned aerial vehicle using FlightGear. In *AIAA Infotech@Aerospace 2005 Conference and Exhibit*, AIAA 2005-7083, Arlington, VA, Sept. 26-29 2005.

[43] FlightGear official website: http://www.flightgear.org/.

[44] Rasmussen, S.J. and Breslin, G.B. AVDS: a flight systems design tool for visualization and engineer-in-the-loop simulation. In *AIAA Guidance, Navigation, and Control Conference and Exhibit*, AIAA 1997-3467, New-Orleans, LA, Aug. 11-13 1997.

[45] AVDS official website: http://www.rassimtech.com/.

[46] Kurylowich, G. A method for assessing the impact of wake vortices on USAF operations. Technical Report AFFDL-TR-79-3060, Air Force Flight Dynamics Laboratory, Wright-Patterson Air Force Base, OH 45433, Jul. 1979.

[47] ASTRAEA website: http://www.projectastraea.co.uk/.



https://dspace.org/

Simulation of wake vortex effects for UAVs in close formation flight

Saban, Deborah; Whidborne, James F.; Cooke, Alastair K.

2009-11-30T00:00:00Z
Royal Aeronautical Society
http://dspace.lib.cranfield.ac.uk/handle/1826/7613
D. Saban, J.F. Whidborne. Simulation of wake vortex effects for UAVs in close formation flight. Aeronautical Journal, 2009, Volume 113, Issue 1149, pp727-738

Downloaded from a DSpace repository. https://dspace.org/